Regional surface soil heat flux estimate from multiple remote sensing data in a temperate and semiarid basin

Li, Nana; Jia, Li; Lu, Jing; Menenti, Massimo; Zhou, J.

DOI
10.1117/1.JRS.11.016028

Publication date
2017

Document Version
Final published version

Published in
Journal of Applied Remote Sensing

Journal of
Applied Remote Sensing

RemoteSensing.SPIEDigitalLibrary.org

Regional surface soil heat flux estimate from multiple remote sensing data in a temperate and semiarid basin

Nana Li
Li Jia
Jing Lu
Massimo Menenti
Jie Zhou

SPIE.

Nana Li, Li Jia, Jing Lu, Massimo Menenti, Jie Zhou, "Regional surface soil heat flux estimate from multiple remote sensing data in a temperate and semiarid basin," *J. Appl. Remote Sens.* **11**(1), 016028 (2017), doi: 10.1117/1.JRS.11.016028.

Regional surface soil heat flux estimate from multiple remote sensing data in a temperate and semiarid basin

Nana Li,[a,b,c] Li Jia,[a,c,*] Jing Lu,[a,c] Massimo Menenti,[a,d] and Jie Zhou[a]

[a]Chinese Academy of Sciences, Institute of Remote Sensing and Digital Earth, State Key Laboratory of Remote Sensing Science, Beijing 100101, China

[b]Tsinghua University, Department of Hydraulic Engineering, State Key Laboratory of Hydroscience and Engineering, Beijing 100084, China

[c]Joint Center for Global Change Studies, Beijing 100875, China

[d]Delft University of Technology, Department of Geosciences and Remote Sensing, Stevinweg 1, Delft 2628 CN, The Netherlands

Abstract. The regional surface soil heat flux (G_0) estimation is very important for the large-scale land surface process modeling. However, most of the regional G_0 estimation methods are based on the empirical relationship between G_0 and the net radiation flux. A physical model based on harmonic analysis was improved (referred to as "HM model") and applied over the Heihe River Basin northwest China with multiple remote sensing data, e.g., FY-2C, AMSR-E, and MODIS, and soil map data. The sensitivity analysis of the model was studied as well. The results show that the improved model describes the variation of G_0 well. Land surface temperature (LST) and thermal inertia (Γ) are the two key input variables to the HM model. Compared with *in situ* G_0, there are some differences, mainly due to the differences between remote-sensed LST and the *in situ* LST. The sensitivity analysis shows that the errors from −7 to −0.5 K in LST amplitude and from −300 to 300 $\mathrm{J\,m^{-2}\,K^{-1}\,s^{-0.5}}$ in Γ will cause about 20% errors, which are acceptable for G_0 estimation.
 [DOI: 10.1117/1.JRS.11.016028]

Keywords: harmonic analysis model; regional soil heat flux; thermal inertia; remote sensing data; arid and semiarid area.

Paper 16300 received Apr. 20, 2016; accepted for publication Jan. 10, 2017; published online Feb. 17, 2017.

1 Introduction

The at-surface soil heat flux, G_0, is an important component of the land surface energy balance, particularly in the condition of dry soil or sparse canopies where G_0 can be as large as 50% of net radiation flux (R_n).[1,2] G_0 can be comparable with the maximum sensible heat flux (H) for well-watered conditions and be nearly the same as the maximum latent heat flux (LE) for senescent vegetation.[3] Many studies have proved that the incorrect estimation of G_0 is also an important factor leading to the surface energy imbalance problem. For example, Wilson et al.[4] revealed that the energy balance closure error for agricultural, grassland, and chaparral land surfaces was reduced by 20% when G_0 was used instead of being measured by soil heat flux plate buried in some depth in the soil. Heusinkveld et al.[5] proved that the energy balance closure error in an arid region became negligible with correct G_0 measurement. Wang et al.[6] found that the energy balance closure underestimation decreased from 32% to 14% when using G_0 (which was calculated by thermal diffusion equation) instead of using the heat flux plate measurements in depth of soil. Thus, the correct determination of G_0 is very important for improving the closure of surface energy balance.[7,8] The regional estimation of G_0 is urgently needed for the regional evapotranspiration estimation and the verification of regional or global circulation models.[9] Many empirical methods have been developed to derive regional G_0 from remotely sensed variables such as net radiation,[10–12] vegetation index,[11,13] land surface temperature (LST),[14] and land surface albedo.[14] The majority of the methods focused on developing the relationship between the ratio of G_0/R_n

*Address all correspondence to: Li Jia, E-mail: jiali@radi.ac.cn

1931-3195/2017/$25.00 © 2017 SPIE

and remote sensing variables. For example, Reginato et al.[15] built a linear relationship between G_0/R_n and vegetation height; Choudhury et al.[10] related G_0/R_n to leaf area index using Beer's law; Su[13] estimated G_0/R_n from fractional vegetation cover. However, those methods ignored the important effect of soil thermal properties on G_0 explicitly, and did not consider the effect of the LST on G_0. Santanello and Friedl[12] determined the diurnal course of G_0/R_n using a cosine model that relates the maximum daytime G_0/R_n to the daily maximum and minimum LSTs. Although LST (usually defined as a composite temperature of vegetation canopy and soil when vegetation exists) was utilized, this method is only applicable to dry and bare soil or dry and sparse canopy areas.[8,16] Bastiaanssen et al.[14] developed another empirical approach to estimate G_0/R_n from LST, normalized difference vegetation index (NDVI), and land surface albedo assuming both LST and albedo reflect land surface wetness. However, neither the land surface albedo nor LST retrieved from remote sensing data can accurately reflect the soil wetness under dense vegetation conditions. However, the soil wetness is important for soil thermal properties and soil temperature. Cammalleri et al.[17] introduced a correction factor to explicitly incorporate the soil water content behavior. Based on the previous work (e.g., Carslaw and Jaeger,[18] Van Wijk and DeVries,[19] Horton and Wierenga[20]), Murray and Verhoef[8,16] proposed a physically based model using the harmonic analysis of soil surface temperature to estimate G_0 (HM model hereinafter), which is independent of net radiation flux R_n. In the HM model, the input variables include soil surface temperature, soil surface moisture, and fractional vegetation cover. These variables can be obtained from satellite observations, which make the model promising for the regional G_0 estimate. In addition, errors and uncertainties on G_0 are more transparent and more easily interpreted in Murray's HM model. However, there are still some disadvantages in the HM model. First, a fixed value of phase shift between canopy composite temperature and below-canopy soil surface temperature is used in the HM model, while it may vary with the underlying surfaces. Second, the HM model uses empirical and simulated soil properties, so it needs more discussion since soil properties vary with time and space. Moreover, in addition to the study of Verhoef et al.,[9] the HM model has not yet been applied at the regional scale using remote sensing data.

To improve the application of the HM model at the regional scale, the objectives of this study are: (1) to develop a parameterization of the phase shift between canopy composite temperature and below-canopy soil surface temperature rather than using a fixed value as in the original scheme; (2) to obtain soil properties (soil porosity and sand fraction) from a soil map to replace the empirical and simulated ones; (3) to estimate regional G_0 in the Heihe River Basin (HRB) using multisource remote sensing data including visible, thermal infrared, and microwave remote sensing data; (4) to perform a sensitivity analysis of the HM model to input variables and clarify which variables are significant for G_0 estimate.

2 Materials and Methods

2.1 *Study Area*

The HRB is located in arid and semiarid regions of northwest China. The study area is located in the upper and middle reach of HRB (Fig. 1). The HRB is a typical inland river basin in China with a geographic range between 37.5 to 42.2°N and 97.1 to 102.0°E, and with an area of about 14×10^4 km^2. It has a unique mixed landscape of "ice/frozen soil–forest–river and wetland–oasis–desert" and complicated ecohydrological processes.[21] The upper reach lies in the Qilian Mountains with an elevation of about 3000 to 5000 m and is mainly covered by forest, shrubs, and alpine meadows with an average annual air temperature, annual precipitation, and relative humidity of 2.0°C, 350 mm, and 60% (from 1960 to 2000), respectively.[22] The middle reach is flat with an elevation between 1400 and 1700 m and is mainly irrigated farmland; from east to west the mean annual air temperature is about 2.8°C to 7.6°C and precipitation is 250 to 50 mm (1960 to 2000). Ground measurements in two experimental sites were used in this study. The Yingke site (100° 24' 37" E, 38° 51' 26" N) is located in the middle reach of the HRB with maize and spring wheat from May to July, maize only in August to September, and bare soil (loamy soils) in the remaining period. The maximum height of maize canopy is 1.8 m and that of spring wheat is about 1 m in the growing season.[23,24] The Arou site lies in the upper reach of the HRB and is covered with grass in the growing season from May to September with 0.2 to 0.3 m height on sandy soils.

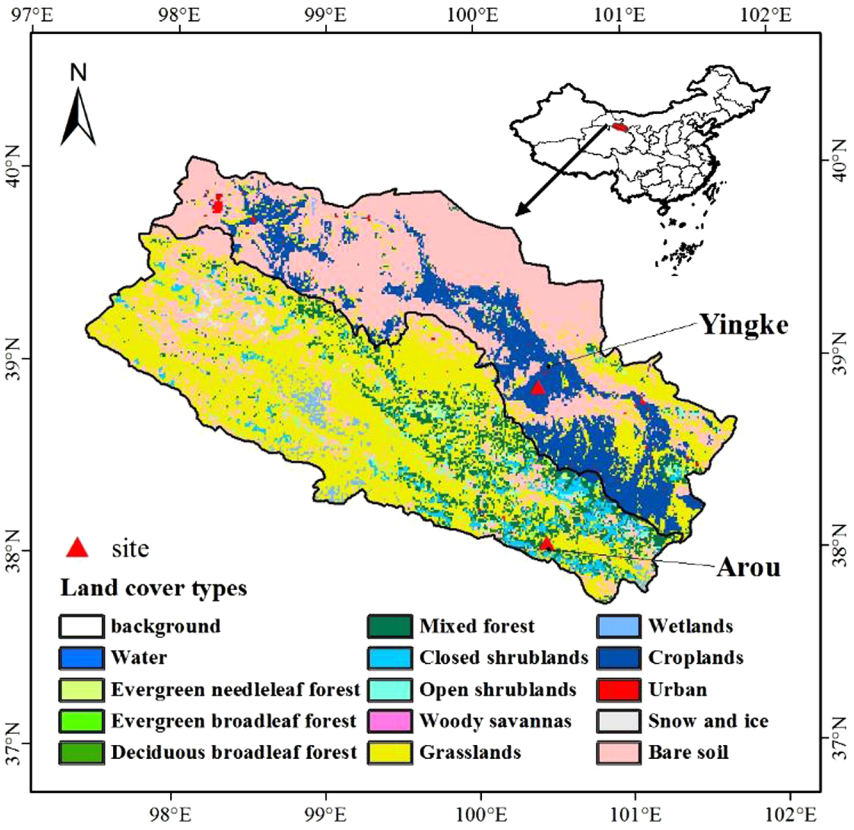

Fig. 1 The land cover map of upper and middle reaches of the HRB in 2010.

2.2 *Data*

2.2.1 *Remote sensing data and soil map*

The forcing data of the HM model include LST, surface soil moisture, and fractional vegetation cover f_c, which can be derived from remote sensing data. Relevant surface properties are soil porosity and soil texture, which can be obtained from a soil map. Table 1 gives the summary of the remote sensing data and soil map used for regional scale application in this paper. The LST was retrieved from Chinese Geostationary Meteorological Satellite Feng Yun (FY-2C) using a generalized split-window algorithm[25,26] and gap-filled by applying the harmonic analysis of time series (HANTS) and multichannel singular spectrum analysis methodology.[27,28] The dataset was provided by the EU-FP7 project CEOP-AEGIS.[29] The hourly LST was then linearly interpolated to 30-min intervals in this study. The soil moisture product produced by Liu et al.[30] is retrieved from the observations by AMSR-E (Advanced Microwave Scanning Radiometer for EOS) sensor using a new dual-channel algorithm based on the Q_p model developed by Shi et al.[31,32] Compared with ground measurements, the new soil moisture product performs better than the NASA product of AMSR-E, with a root mean square error (RMSE) improved from 0.066 to 0.048 $cm^3\ cm^{-3}$ and a coefficient of determination (R^2) from 0.08 to 0.59. Moreover, the new soil moisture product reveals the seasonal variation of soil moisture better than the NASA product. The cloud-free NDVI time series are reconstructed based on the MODIS NDVI product using the improved HANTS method (iHANTS),[33,34] and the data can be found in the Cold and Arid Regions Science Data Center at Lanzhou.[35] This gap-free NDVI dataset is employed in this paper to calculate f_c as $f_c = 1 - [(\mathrm{NDVI}_{\max} - \mathrm{NDVI})/(\mathrm{NDVI}_{\max} - \mathrm{NDVI}_{\min})]^{0.7}$, where $\mathrm{NDVI}_{\max}$ and $\mathrm{NDVI}_{\min}$ are NDVI values for full vegetation cover and bare soil, respectively.[36] The soil properties are taken from a soil map produced by Shangguan et al.[37] The remote sensing data in May and July of 2009 were selected and unified to 1-km spatial resolution with a bilinear interpolation method.

Table 1 Remote sensing data and soil map used in the present study.

Data	Satellite/other source	Spatial resolution	Temporal resolution
NDVI	MODIS-Terra	1 km	Daily
Soil moisture	AMSR-E	0.25 deg	Twice a day
Land surface temperature	FY-2C	5 km	Hourly
Soil texture and porosity	Soil map	30 arc sec	Perennially

Table 2 Variables measured and the depths/heights of the sensors at the Yingke and Arou sites in the HRB in 2009 (according to Liu et al.[23,24]).

Variables	Yingke site (m)	Arou site (m)
Soil temperature	0.1, 0.2, 0.4, 0.8, 1.2, 1.6 (109, Campbell)	0.1, 0.2, 0.4, 0.8, 1.2, 1.6 (107, Campbell)
Soil moisture	0.1, 0.2, 0.4, 0.8, 1.2, 1.6 (CS616, Campbell)	0.1, 0.2, 0.4, 0.8, 1.2, 1.6 (CS616, Campbell)
Upward/downward long wave radiation fluxes	4 (CG3, Kipp, and Zonen)	1.5 (PIR, Eppley)

2.2.2 *In situ data*

Since the 1980s, many comprehensive hydrological and ecological experiments have been carried out in the HRB, e.g., the HRB field experiment (HEIFE),[38,39] Watershed Allied Telemetry Experimental Research (WATER),[40–42] and the Heihe Watershed Allied Telemetry Experimental Research (HiWATER).[21,43] The *in situ* micrometeorological data at the Yingke and Arou sites are from WATER in 2009 with 30-min intervals and are provided by the Cold and Arid Regions Science Data Center at Lanzhou.

The *in situ* G_0 measurements in this study were calculated by the thermal diffusion equation[44] with measurements of soil temperature and moisture profiles at the Yingke and Arou sites (Table 2). The *in situ* LST required in the thermal diffusion equation is derived from upward and downward longwave radiation fluxes [Eq. (7)].

2.3 *Methods*

2.3.1 *HM model*

The physical model for the land surface soil heat flux estimate based on the harmonic analysis of soil surface temperature (HM model) is described by Murray and Verhoef[8,16] as follows:

$$G_0 = \Gamma \cdot \sum_{n=1}^{M} A_n \sqrt{n\omega} \sin\left(n\omega t + \phi_n + \frac{\pi}{4}\right) = \Gamma \cdot J_s, \tag{1}$$

where G_0 (W m^{-2}) is the at-surface soil heat flux, Γ (J m^{-2} K^{-1} s$^{-0.5}$) is the soil thermal inertia, M is the total number of harmonics used ($M = 10$ in this study), A_n is the amplitude of the n'th soil surface temperature (T_s) harmonic, ω (rad s^{-1}) is the angular frequency, t is the time (s), ϕ_n (rad) is the phase shift of the n'th soil surface temperature harmonic, and J_s is the summation of harmonic terms of soil surface temperature.

The parameter soil thermal inertia, Γ, is a key variable for estimating G_0 using Eq. (1). Murray and Verhoef[8] adopted the concept of normalized thermal conductivity[45] and developed a physical method to calculate Γ as

$$\Gamma = \exp[\gamma \cdot (1 - S_r^{\gamma-\delta})] \cdot (\Gamma_* - \Gamma_0) + \Gamma_0, \tag{2}$$

where Γ_* and Γ_0 are the thermal inertia for saturated and air-dry soil ($\mathrm{J\,m^{-2}\,K^{-1}\,s^{-0.5}}$), respectively, and can be calculated as $\Gamma_* = 788.2 \cdot \theta_*^{1.29}$ and $\Gamma_0 = -1062.4 \cdot \theta_* + 1010.8$ with θ_* ($\mathrm{cm^3\,cm^{-3}}$) as soil porosity (equal to the saturated soil moisture content); γ (−) is a parameter depending on soil texture; S_r ($\mathrm{cm^3\,cm^{-3}}$) is relative saturation and is equal to θ/θ_*, with θ ($\mathrm{cm^3\,cm^{-3}}$) as actual soil moisture; and δ (−) is a shape parameter.

With remote sensing observations by space-borne or ground-based radiometers, usually the composite temperature of soil and vegetation canopy is measured for vegetated land surfaces other than soil only. Assuming the same time offset Δt (s) applies to all harmonics, J_s is written as

$$J_s(t) = \left(1 - \frac{1}{2} \cdot f_c\right) \cdot \sum_{n=1}^{M} \left[A_n' \sqrt{n\omega} \cdot \sin\left(n\omega t + \Phi_n' + \frac{\pi}{4} - \frac{\pi \cdot \Delta t}{12}\right)\right], \tag{3}$$

where f_c is fractional vegetation cover, A_n' (K) and ϕ_n' (rad) are the daily amplitude and phase shift of the n'th canopy composite temperature harmonic, respectively. Δt (s) is the time offset between the canopy composite temperature and the below-canopy soil surface temperature and is found as 1.5 h in Murray and Verhoef based on their data.[8] In this paper, we propose a simple parameterization to estimate this time offset Δt by taking into account the effect of vegetation condition (see Sec. 2.3.2).

2.3.2 *Parameterization of time offset*

Murray and Verhoef[16] and Verhoef et al.[9] showed that the below-canopy soil surface temperature arrived at the daily maximum a few hours later than canopy composite temperature according to their field data due to the extinction by the vegetation canopy. Such time offset between the canopy composite temperature and the below-canopy soil surface temperature results in the delayed maximum daily surface soil flux G_0 for vegetated surface when compared with bare soil surface. They also showed that a constant value 1.5 h was sufficient for various canopy densities (observed f_c ranged from 0.6 to 0.99) and canopy types (oilseed rape, winter wheat, spring wheat, and borage). Theoretically, the time offset depends on canopy density and canopy structure.[9] According to measurements in July at the Yingke site in the HRB, the time offset (Δt) value of 1.5 h is applicable for full covered vegetation canopy (i.e., $f_c = 1$) but not for sparse canopy, and Δt is equal to zero for bare soil ($f_c = 0$). Although canopy structure influences the radiation extinction, only fractional vegetation cover f_c is used to represent the canopy condition in the present study. With the two boundary values (i.e., $\Delta t = 1.5$ h for $f_c = 1$ and $\Delta t = 0$ h for $f_c = 0$), a linear approach is proposed here to describe the time offset Δt as a function of f_c:

$$\Delta t = 1.5 \cdot f_c \tag{4}$$

2.3.3 *Sensitivity coefficient*

Sensitivity analysis is important for understanding the source of uncertainties in hydrological and ecological modeling studies;[46,47] in particular, in this study it can identify which input parameter most affects G_0 estimate. A simple method is to plot the relative changes of a dependent variable against the relative changes of an independent variable as a curve.[48,49] Nevertheless, a mathematically defined sensitivity coefficient is mostly used in sensitivity

analysis.[47,50–53] It is difficult to compare the sensitivity of variables by partial derivatives for a multivariables model (e.g., Penman–Monteith method). A nondimensional sensitivity coefficient is a transform of the partial derivative approach, which has been widely used in evapotranspiration studies.[52–55] The sensitivity coefficient is as follows:[52]

$$S_{V_i} = \lim_{\Delta V_i \to 0} \left(\frac{\Delta G_0 / G_0}{\Delta V_i / V_i} \right) = \frac{\partial G_0}{\partial V_i} \cdot \frac{V_i}{G_0}, \tag{5}$$

where S_{Vi} is the sensitivity coefficient and V_i is the i'th variable. A positive/negative sensitivity coefficient indicates G_0 will increase/decrease as the variable increases. The larger the sensitivity coefficient is, the larger effect of the given variable on G_0.

The relative error (RE) is used to evaluate variation in G_0, as follows:

$$\mathrm{RE} = \frac{G_0' - G_0}{G_0} \times 100\%, \tag{6}$$

where RE is the RE of G_0, G_0' is G_0 with varying LST or Γ, and G_0 is the original value.

2.3.4 *In situ LST*

The *in situ* LST is calculated as follows:

$$T(z_0) = \left[\frac{R_{L\uparrow} - (1-\varepsilon) R_{L\downarrow}}{\varepsilon \sigma} \right]^{1/4}, \tag{7}$$

where $R_{L\uparrow}$ and $R_{L\downarrow}$ are the upward and downward longwave radiation fluxes ($\mathrm{W\,m^{-2}}$), respectively, ε is the land surface emissivity (taken as 0.987 at the Yingke and Arou sites),[23,24] and the Stefan–Boltzmann constant $\sigma = 5.67 \times 10^{-8}$ ($\mathrm{W\,m^{-2}\,K^{-4}}$).

3 Results and Discussion

3.1 *In Situ Soil Heat Fluxes with Different Time Offsets*

The surface soil heat flux estimated by the HM model [Eq. (1) with $M = 10$], with time offset of 1.5 h and $1.5 f_c$ h using *in situ* micrometeorological measurements in May and July of 2009 at the Yingke site, were compared with the *in situ* G_0 measurements. To show the difference in the estimated G_0 with different time offsets more clearly, only some days with varying f_c (14, 22, 23, 25, 28, 29, 30 in May and 17, 19, 21, 23, 24, 26, 28 in July of 2009) were selected, as shown in Fig. 2. G_0 estimation with time offset of 1.5 h are lagged G_0 with $1.5 f_c$ h in May, and they are nearly the same in July (Fig. 2). RMSE is improved from 80.8 to 52.8 $\mathrm{W \cdot m^{-2}}$ when using time offset of $1.5 f_c$ h instead of 1.5 h in whole May [Fig. 3(a)], and R^2 increases from 0.59 to 0.83. However, the improvement is not obvious in July, with nearly the same RMSE and R^2 [Fig. 3(b)]. Thus, the improved model improves the accuracy of G_0 for sparse vegetation in May when the mean f_c was about 0.3. Furthermore, the results in July are not better than May, and the HM model for vegetated surface should be improved further in our following work. At the Arou site, f_c had less variation over the whole year than that at the Yingke site. In conclusion, the improvement performs better at the Yingke site than at the Arou site, which is not shown here.

3.2 *Spatial Distribution of G_0*

The improved HM model [Eqs. (3) and (4)] was applied to remote sensing data in the HRB region, as listed in Table 1. To analyze the spatial patterns of the estimated G_0 in different seasons, G_0 at the same time on different days over a month were averaged to avoid the

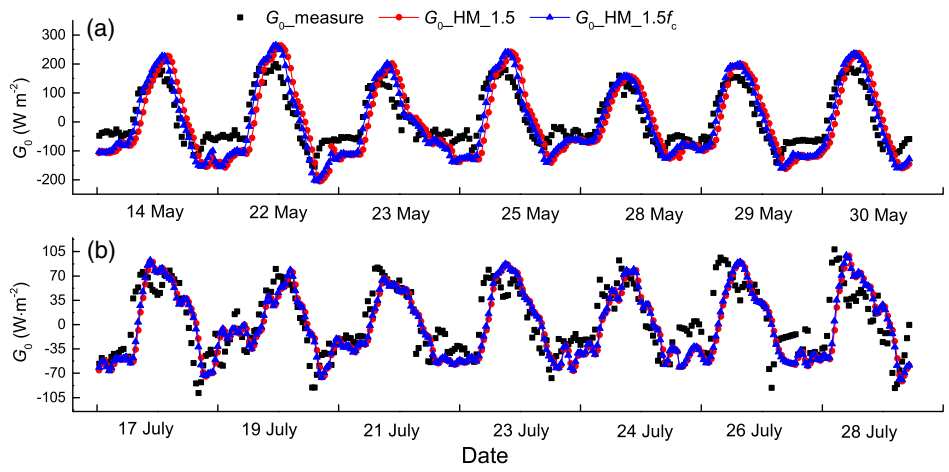

Fig. 2 The diurnal variations of G_0 on some days in (a) May and (b) July of 2009 at the Yingke site. G_0_measure is the *in situ* measurements of surface soil heat flux, G_0_HM_1.5 and G_0_HM_1.5f_c are calculated by HM model with time offset of 1.5 h and 1.5f_c h, respectively, using *in situ* measurements of LST.

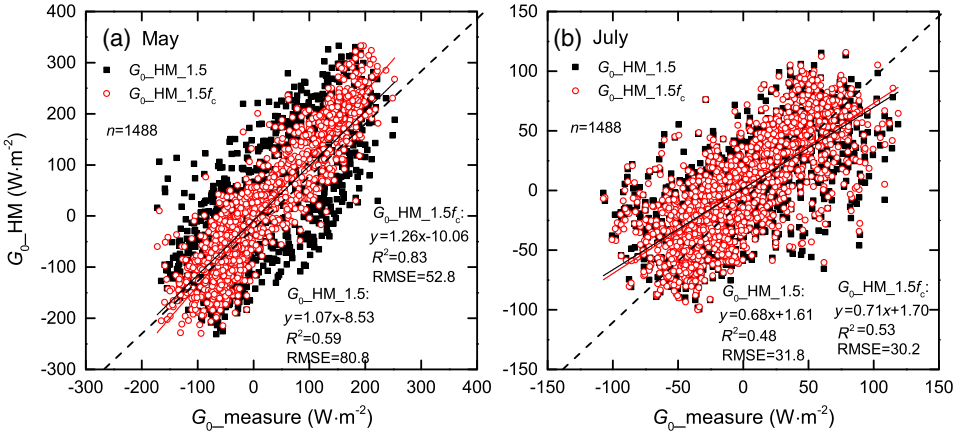

Fig. 3 Scatter plot of G_0 measurement and G_0 estimation by HM model in the whole (a) May and (b) July of 2009 at the Yingke site. G_0_measure, G_0_HM_1.5, and G_0_HM_1.5f_c are the same as in Fig. 2.

contingency caused by gaps in the remote sensing data due to cloud cover and other reasons. The mean monthly G_0 maps at 10:30 am in May and July are shown in Fig. 4. As expected, it is found that the G_0 values are generally higher in bare soil than in vegetated surfaces [Figs. 4(a) and 4(b)] in both May and July of 2009. More energy was transferred into the soil directly for bare surfaces, while for vegetated surface the energy is intercepted by vegetation canopy for transpiration, so less energy was conducted into the soil. The G_0 values over the desert area in the center of the middle reach are significantly higher than the values in the surrounding bare soil in both May and July of 2009 due to higher sand fraction and lower porosity in desert area, according to the soil map, which gives higher thermal inertia according to Eq. (2) [Figs. 4(c) and 4(d)].

For the same land cover type, the G_0 values vary with f_c from May to July. The mean G_0 values in May are 222 W m^{-2} at the Yingke site and 156 W m^{-2} at the Arou site, while the mean values of G_0 in July are 103 and 87 W m^{-2} at the two sites, respectively. In both sites, the G_0 values are lower in July due to higher f_c over maize and grass land surfaces in May than in July. The f_c increased from 0.32 to 0.77 from May to July at the Yingke site and from 0.46 to 1.0 at the Arou site in 2009.

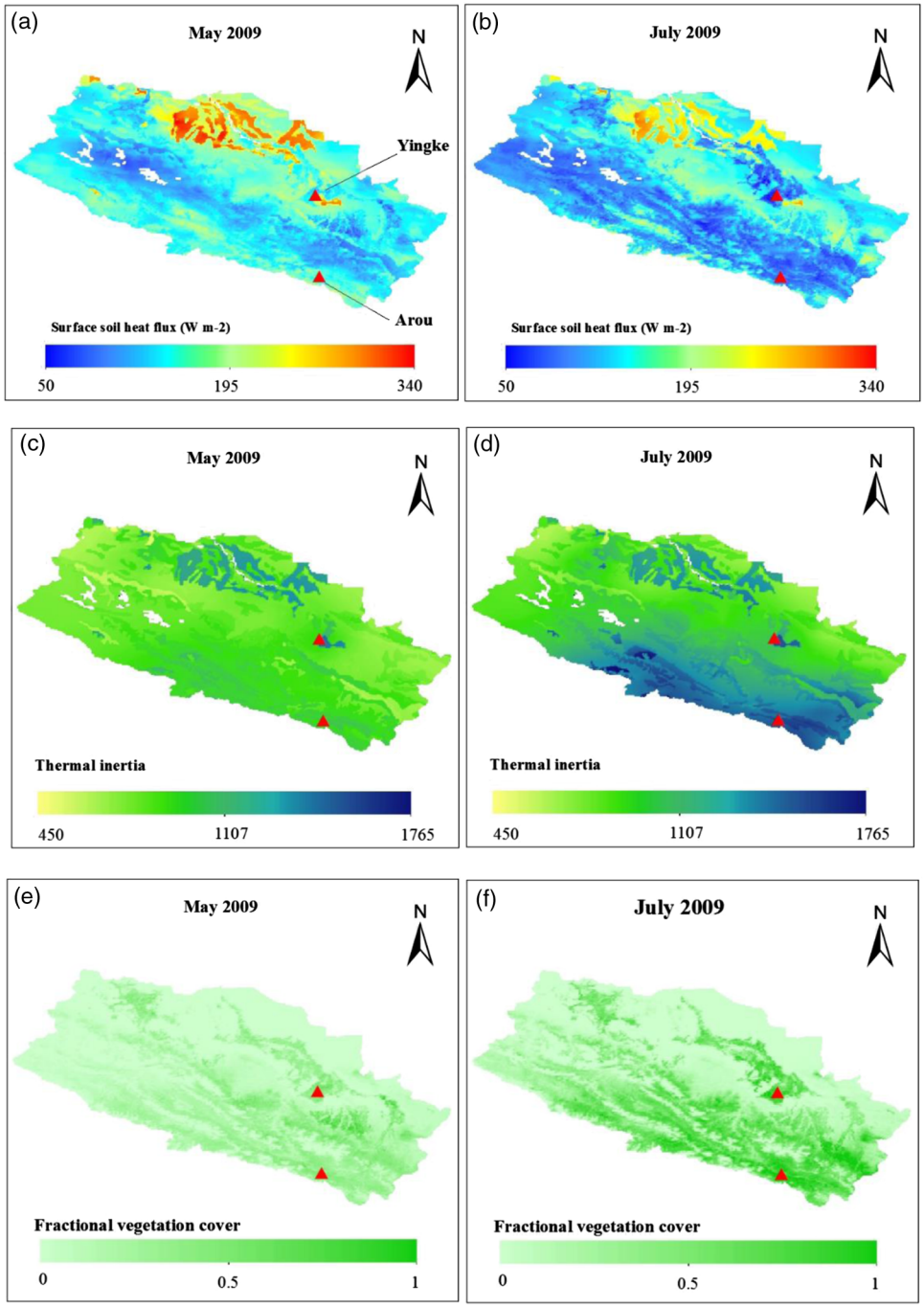

Fig. 4 The distribution of mean monthly G_0 estimation at 10:30 am local time (a) in May and (b) in July, the distribution of mean monthly thermal inertia (c) in May and (d) in July, and the distribution of monthly f_c (e) in May and (f) in July in 2009 in the upper and middle reaches of the HRB.

In July of 2009, the maximum of monthly G_0 value in the study area at 10:30 am can reach to 329 $\mathrm{W\,m^{-2}}$ in desert area in the middle reach of HRB, where R_n is about 600 $\mathrm{W\,m^{-2}}$. This leads to G_0 being up to 50% of R_n. The G_0 for the cropland in the middle reach is higher in May than that in July as the cropland is at the emergence stage in May with a lower f_c [Fig. 4(e)]. The G_0 for the vegetated surfaces in the upper reach in July is lower than in May, which is attributed to higher f_c for grass land in the growing season [Fig. 4(f)].

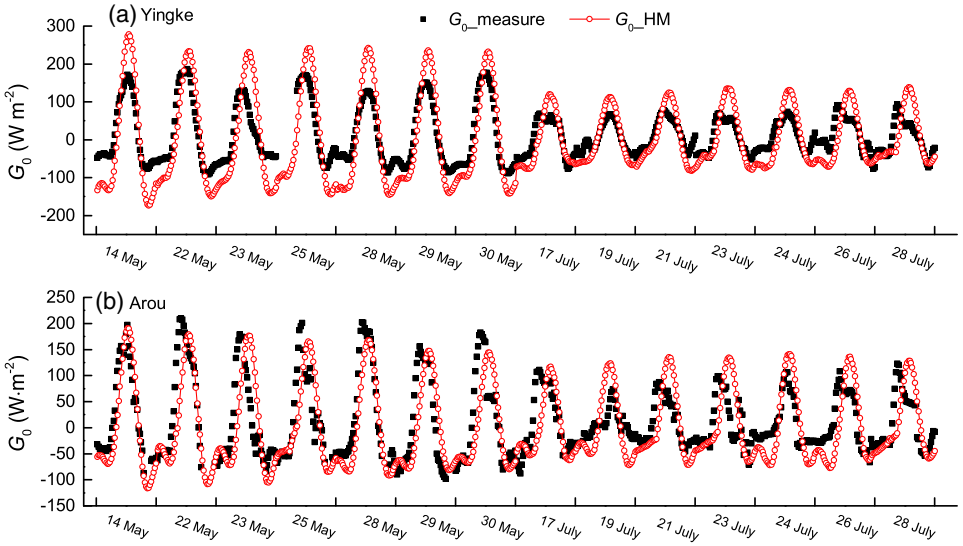

Fig. 5 The diurnal variations of land surface soil heat flux G_0 in May and July of 2009: (a) at the Yingke site and (b) at the Arou site. G_0_HM is calculated by the improved HM model using remote sensing data and soil map data.

3.3 *Validation of Estimated Soil Heat Flux from Remote Sensing*

The calculated G_0 by the improved HM model using remote sensing data and soil map was evaluated at the Yingke and Arou sites by comparing *in situ* G_0 measurements. It was found that the estimated G_0 is overestimated in both daytime and nighttime at the Yingke site [Fig. 5(a)]. At the Arou site, the estimated daytime G_0 (positive) is underestimated in May and overestimated in July [Fig. 5(b)]. The deviations are mainly caused by remote sensing data, which are different from ground measurements. To investigate which remote sensing data lead to G_0 errors the most, cross-calculation with remote sensing data and *in situ* measurements were performed in this study.

As shown in Table 3, four different variables were applied to the HM model. *A*, *B*, *C*, and *D* in Table 3 represent LST from FY-2C, the *in situ* LST derived from the observed longwave radiation, the thermal inertia from AMSR-E data and soil map, and the *in situ* thermal inertia derived from the observed soil properties, respectively. It is important to know which forcing data caused the overestimation or underestimation in the calculated G_0 when applying the HM model to remote sensing data. Equation (1) shows that the thermal inertia and LST affect G_0 directly. Compared to G_0 estimated with *A* and *C*, the G_0 estimated with *B* and *C* is more consistent with *in situ* G_0 measurements (Fig. 6). The R^2 increased from 0.80 to 0.84 at the Yingke site and from 0.54 to 0.72 at the Arou site. The RMSE also increased from 48.2 to 37.4 W m^{-2} at the Yingke site and from 52.4 to 33.2 W m^{-2} at the Arou site. Although G_0 estimated with *A* and *D* is also improved, the improvement is not so obvious. It shows that the deviation of estimated G_0 using remote sensing data is mainly caused by the difference between remotely sensed LST and ground-measured LST, and the AMSR-E soil moisture and soil texture bring fewer errors.

Table 3 The combinations of LST and Γ derived from remote sensing data and *in situ* measurements, respectively.

Variable	Remote sensing data	*In situ* measurement
LST	*A*: FY-2C	*B*: field LST
Γ	*C*: AMSR-E, soil map	*D*: field soil moisture, soil texture

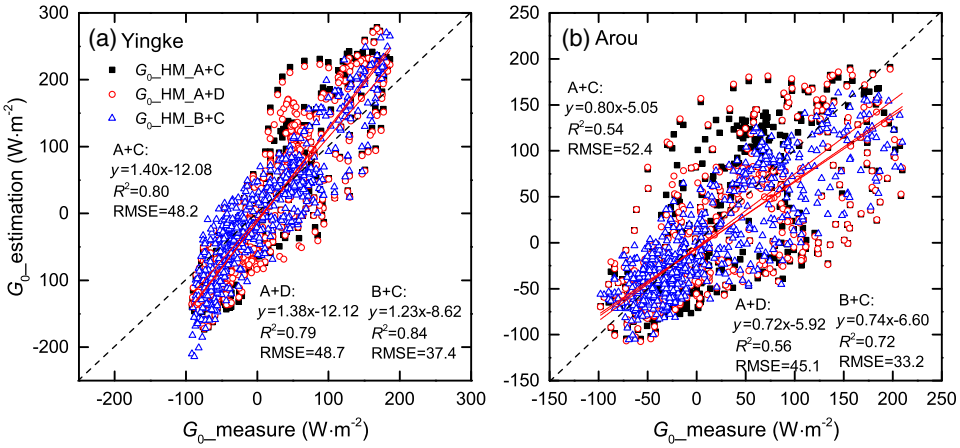

Fig. 6 Scatterplot of G_0 estimation for cases *A*, *B*, *C*, and *D* in Table 3 versus *in situ* G_0 measurement, respectively, on 14 days (14, 22, 23, 25, 28, 29, 30 in May and 17, 19, 21, 23, 24, 26, 28 in July of 2009) (a) at the Yinke site and (b) at the Arou site.

3.4 *Sensitivity of Estimated G_0 to Input Variables*

3.4.1 *Sensitivity coefficients for each variable*

The estimated G_0 is related to LST, soil moisture, f_c, and soil properties, which have different dimensions and different ranges of values. The input variables are interrelated and the question arises as to which parameter is more influential on the estimated G_0. Sensitivity analysis can answer the question. According to Eq. (5), the sensitivity coefficients for the input variables were evaluated and are listed in Table 4. The data used to perform the sensitivity analysis are from the Yingke site. The LST, soil moisture, and sand fraction are positively correlated to G_0, while f_c and porosity are negatively correlated to G_0. Notably, the porosity is the most influential on G_0, and sand fraction is the least important with a sensitivity coefficient of 0.06. f_c is more related to G_0 for dense vegetation, which shows that the relationship of f_c and G_0 is nonlinear.

3.4.2 *Sensitivity of G_0 to LST and thermal inertia*

According to the HM model, G_0 values depend on the amplitude of LST and thermal inertia. The sensitivity coefficients give the qualitative dependence of G_0 on input variables. This section presents the quantitative sensitivity analysis of G_0 to the amplitude of LST and thermal inertia. With a fixed thermal inertia, G_0 was calculated using varied LST with daily amplitude $(A) \pm dA$ $(dA = -12, -11, -9, -7, -6, -2, -0.5, 1, 3, 5$ K). Similarly, with a fixed LST, G_0 was calculated using varied thermal inertia values $\Gamma \pm d\Gamma$ $(d\Gamma = -1000, -800, -600, -400, -200, 0, 200, 400, 600, 800, 1000$ J m^{-2} K^{-1} s$^{-0.5}$) by the HM model. The RE is used to evaluate G_0 variation based on Eq. (6).

Table 4 The sensitivity coefficients of input variables in the HM model.

Variables	S_{Vi}
Amplitude of LST	0.99
Soil moisture	0.44 to 0.46
f_c	−0.18 to −0.69
Porosity	−1.3
Sand fraction	0.06

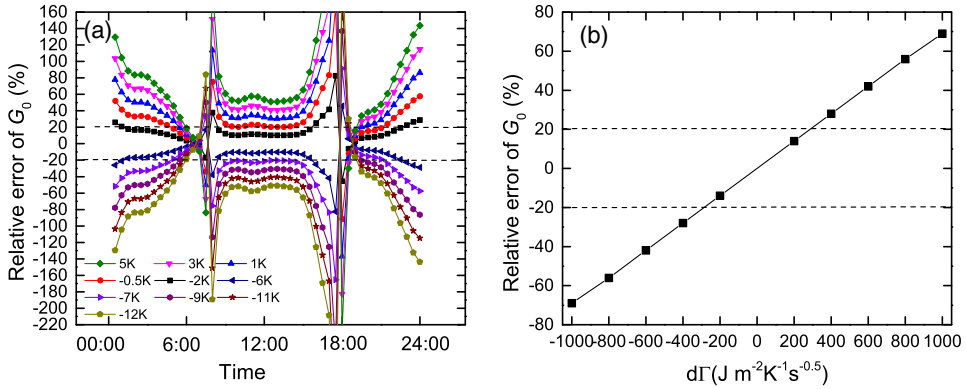

Fig. 7 The mean RE on G_0 in 14 days (14, 22, 23, 25, 28, 29, 30 in May and 17, 19, 21, 23, 24, 26, 28 in July of 2009) with (a) varied amplitude of LST and (b) varied thermal inertia at the Yingke site.

G_0 is nonlinearly correlated to LST amplitude and linearly correlated to thermal inertia. Therefore, RE value is constant in each day with the same $d\Gamma$. However, RE is varied with the same dA. An error of 20% on G_0 evaluation is acceptable.[56–58] When dA is varied from -0.5 to -7 K, and $d\Gamma$ is varied from -300 to 300 J m^{-2} K^{-1} s$^{-0.5}$, respectively, the mean RE on G_0 in the 14 days (14, 22, 23, 25, 28, 29, 30 in May and 17, 19, 21, 23, 24, 26, 28 in July of 2009) is less than 20% at the Yingke site (Fig. 7).

3.4.3 *Sensitivity of thermal inertia to soil properties and soil moisture*

The soil porosity and soil sand fraction, together with soil moisture were used to calculate thermal inertia in the HM model [Eq. (2)]. According to the China soil map used in this study, the soil porosity varies from 0.43 to 0.67 when the sand fraction is less than 0.4, and the sand fraction value is mostly less than 0.8 for soil. The relative saturation S_r ($\theta/\theta*$) describes the soil moisture conditions. The variations of Γ from dry to wet soil conditions are shown in Fig. 8. Different values of soil porosity (0.43, 0.55, and 0.67) when the sand fraction is less than 0.4 were used to calculate Γ under different soil moisture conditions [Fig. 8(a)]. Different values of sand fraction and a fixed soil porosity of 0.46 were also used to calculate Γ [Fig. 8(b)]. It is shown that Γ increases with the increasing soil moisture. Γ varies largely under wet soil conditions (with larger S_r) than dry soil conditions (with smaller S_r) with the same soil porosity variation [Fig. 8(a)], which means that Γ under wet conditions (i.e., when S_r is larger) is more sensitive to soil porosity. Γ is sensitive to smaller porosity, according to Fig. 8(a), because there is greater change of Γ

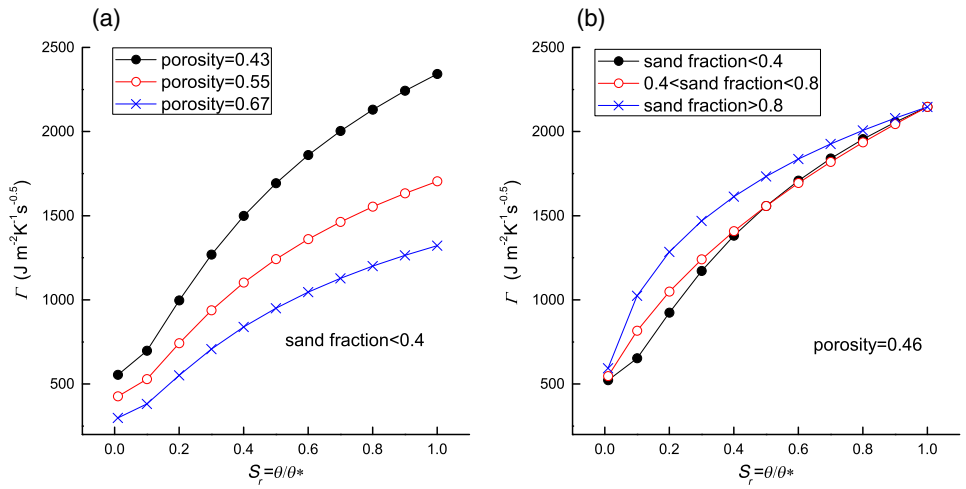

Fig. 8 The sensitivity of thermal inertia as a function of relative saturation (S_r) to (a) porosity and (b) sand fraction.

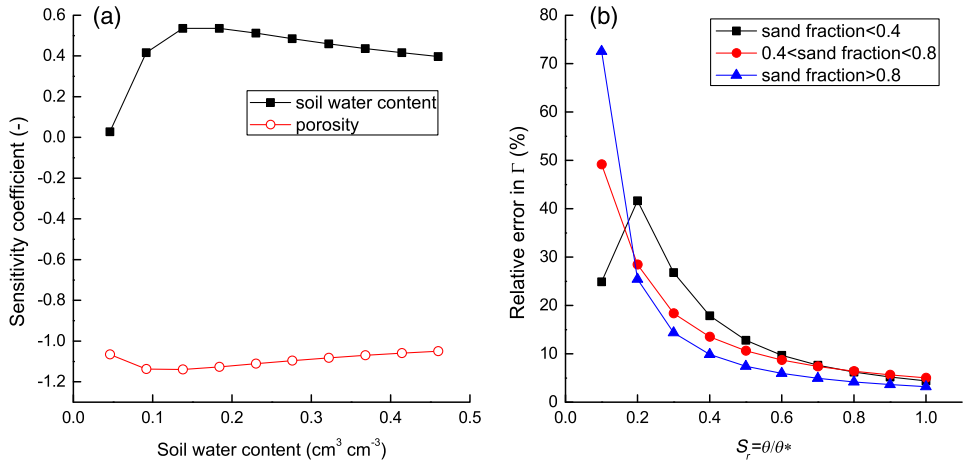

Fig. 9 (a) The sensitivity coefficients of Γ for soil moisture and soil porosity under conditions of sand fraction less than 0.4 soil, (b) the RE in Γ as a function of relative saturation, and (c) the sensitivity coefficients of Γ for sand fraction and soil porosity [the porosity is same as in (a)].

with porosity from 0.43 to 0.55 than that from 0.55 to 0.67 under the same S_r. Figure 8(b) shows that the difference in thermal inertia with varied sand fraction becomes smaller with increasing soil moisture. There is little change in Γ with sand fraction less than 0.8 (which is the dominant case in the Chinese sand fraction distribution). Thus, Γ is more sensitive to porosity than sand fraction in any soil moisture conditions.

The sensitivity coefficients of thermal inertia for soil moisture with a porosity of 0.46 and for porosity varying from 0.46 to 0.67 were calculated under different soil moisture content with a sand fraction less than 0.4 [Fig. 9(a)]. The sensitivity coefficient is positive for soil water content and negative for porosity. Thermal inertia is more sensitive to porosity than soil water content with a maximum sensitivity coefficient of 1.14 versus 0.54. Thus, accurate porosity is most important to estimate thermal inertia. This is also consistent with the results of Lu et al.[59] Figure 9(b) shows the RE in Γ estimate as a function of S_r. The largest RE in Γ is found for soil with sand fraction greater than 0.8 under dry soil conditions ($S_r < 0.1$), whereas the error rapidly declines with increasing values of S_r. The soil with sand fraction between 0.4 and 0.8 shows a steady decline in error. The error for other soils reaches a maximum at $S_r = 0.2$ then drops and under dry soil conditions is smaller than in soils with sand fraction greater than 0.4. This conclusion is consistent with the study of Murray and Verhoef.[8] The thermal inertia has a stronger sensitivity to soil moisture at low values of S_r ($S_r < 0.3$ for soil of sand fraction less than 0.4; $S_r < 0.2$ for other soils) with a more than 20% RE. An RE of 20% in Γ will cause a error of 20% in G_0 based on the HM model. According to the soil moisture category by Murray and Verhoef[8] (dry with $S_r < 0.1$; dry-moist with $0.1 < S_r < 0.25$; moist with $0.26 < S_r < 0.5$; moist-wet with $0.51 < S_r < 0.75$; wet with $0.76 < S_r < 0.1$), for the same soil type, the accurate soil moisture is important for G_0 estimates in dry and dry-moist soil conditions. The sand fraction has a greater effect on Γ for dry and dry-moist soil because the RE in Γ varies largely when different sand fraction is applied [Fig. 9(b)]. That can also be seen obviously in Fig. 9(c): the sensitivity coefficient for sand fraction decreases with increasing S_r and the value is less than 0.2, which is smaller than that for porosity.

3.4.4 *Influence of fractional vegetation cover and satellite zenith angle on G_0*

According to Eqs. (3) and (4), f_c affects not only the amplitude of LST but also the phase of below-canopy soil surface temperature. Thus, if there is a large error on remote sensed f_c, the accuracy of G_0 will be decreased. According to the 30-min interval data in this study, the phase of soil surface temperature can be regarded as invariant when the difference of f_c between remote sensing data and field measurement is less than 0.1 over sparse or dense vegetated surfaces. f_c affects only the amplitude of soil surface temperature and gives less than 10% RE on

G_0. Therefore, if the deviation of f_c is less than 0.1, the impact of the f_c error on G_0 can be neglected.

Murray and Verhoef[16] considered different satellite zenith view angles (β) ranging from 0 deg to 45 deg and found that they bring nearly same J_s and have small effects on G_0. In the present study, FY-2C LST has 40 deg to 45 deg zenith view angles in the HRB area. Thus, the zenith view angle has little effect on G_0 estimation.

4 Conclusions

This study applied the improved physically based HM model based on the one developed by Murray and Verhoef[8,16] to estimate regional G_0 in the HRB. The thermal infrared remote sensing data (LST from FY2C), microwave radiation remote sensing data (surface soil moisture from AMSR-E), visible remote sensing data (NDVI from MODIS), and soil map were used in this study. The improvement is on the parameterization for the phase shift between canopy temperature and below-canopy soil surface temperature by introducing the fractional vegetation cover instead of applying a constant value as in the original model. The improved model was then used to calculate spatiotemporal G_0 in the HRB using satellite data and a soil map. Furthermore, we also studied qualitatively and quantitatively the sensitivity of G_0 to input variables. The main conclusions obtained from the investigation are as follows:

(1) The revised phase of below-canopy soil surface temperature improves the accuracy of G_0 estimation especially over sparsely vegetated surfaces, with R^2 increasing from 0.59 to 0.83 and RMSE decreased from 80.8 to 52.8 $\mathrm{W\,m^{-2}}$ in May of 2009 at the Yingke site.
(2) G_0 varies nonlinearly with the amplitude of LST and linearly with thermal inertia. Compared with G_0 measurement over maize, a variation of -300 to 300 $\mathrm{J\,m^{-2}\,K^{-1}\,s^{-0.5}}$ in thermal inertia and -7 to -0.5 K in the amplitude of LST will cause a less than about 20% RE on the G_0 estimation, which is acceptable.
(3) The soil porosity is the most influential variable on thermal inertia with a maximum sensitivity coefficient of 1.14 under different soil moisture status. The sensitivity of thermal inertia for sand fraction decreases with increasing S_r, and is small when soil is wet. G_0 is more sensitive to soil porosity under wet soil conditions than under dry soil conditions. Thus, the accuracy of porosity is most important for the regional estimate of G_0, especially for wet soil conditions.
(4) The RE in the thermal inertia estimate decreases with increasing S_r. When S_r is less than about 0.3, the RE in the thermal inertia is larger than 20%, which will cause an RE of 20% in G_0 estimate.
(5) The G_0 estimation is more sensitive to f_c for dense vegetation than for sparse vegetation. Approximately 0.1 error in f_c leads to an RE on G_0 of less than 10%. In addition, the effect of the FY-2C view zenith angle of 40 deg to 45 deg on G_0 estimation in the HRB can be neglected.

Appendix: Derivation of LST Amplitudes and Phases of Harmonics

The harmonic analysis of surface temperature is as follows (Horton and Wierenga):[20]

$$T = \bar{T} + \sum_{n=1}^{M} A_n \sin(n\omega t + \phi_n), \tag{8}$$

$$\begin{aligned} A_{\mathrm{n}} \sin(n\omega t + \phi_n) &= A_n \sin(nwt)\cos\phi_n + A_n \cos(nwt)\sin\phi_n \\ &= a_n \sin(nwt) + b_n \cos(nwt), \end{aligned} \tag{9}$$

where $\bar{T}$ is daily average temperature, $a_n = A_n \cos\phi_n$, $b_n = A_n \sin\phi$. a_n and b_n are unknown parameters; other parameters are known. If $M = 10$ and LST is at 30-min timescale (48 data in one day), the expanding Eq. (8) can be expressed as follows:

$$\begin{bmatrix} \sin(wt_1) & \cos(wt_1) & \sin(2wt_1) & \cos(2wt_1) & \sin(3wt_1) & \cos(3wt_1) & \ldots & \sin(10wt_1) & \cos(10wt_1) \\ \sin(wt_2) & \cos(wt_2) & \cos(2wt_2) & \cos(2wt_2) & \sin(3wt_2) & \cos(3wt_2) & \ldots & \sin(10wt_2) & \cos(10wt_2) \\ \vdots & \vdots & \vdots & \vdots & \vdots & \vdots & \vdots & \vdots & \vdots \\ \sin(wt_{48}) & \cos(wt_{48}) & \sin(2wt_{48}) & \cos(2wt_{48}) & \sin(3wt_{48}) & \cos(3wt_{48}) & & \sin(10wt_{48}) & \cos(10wt_{48}) \end{bmatrix} \cdot \begin{bmatrix} a_1 \\ b_1 \\ \vdots \\ b_{20} \end{bmatrix} = \begin{bmatrix} T_1 \\ T_2 \\ \vdots \\ T_{48} \end{bmatrix}, \tag{10}$$

Eq. (10) is written as

$$A \cdot X = Y, \tag{11}$$

where

$$A = \begin{bmatrix} \sin(wt_1) & \cos(wt_1) & \sin(2wt_1) & \cos(2wt_1) & \sin(3wt_1) & \cos(3wt_1) & \ldots & \sin(10wt_1) & \cos(10wt_1) \\ \sin(wt_2) & \cos(wt_2) & \cos(2wt_2) & \cos(2wt_2) & \sin(3wt_2) & \cos(3wt_2) & \ldots & \sin(10wt_2) & \cos(10wt_2) \\ \vdots & \vdots & \vdots & \vdots & \vdots & \vdots & \vdots & \vdots & \vdots \\ \sin(wt_{48}) & \cos(wt_{48}) & \sin(2wt_{48}) & \cos(2wt_{48}) & \sin(3wt_{48}) & \cos(3wt_{48}) & \ldots & \sin(10wt_{48}) & \cos(10wt_{48}) \end{bmatrix}.$$

$$X = \begin{bmatrix} a_1 \\ b_1 \\ \vdots \\ b_{10} \end{bmatrix},$$

$$Y = \begin{bmatrix} T_1 \\ T_2 \\ \vdots \\ T_{48} \end{bmatrix}.$$

$$A^T \cdot A \cdot X = A^T \cdot Y, \tag{12}$$

$$X = (A^T \cdot A)^{-1} \cdot (A^T \cdot Y), \tag{13}$$

where A^T is A matrix transpose, $(A^T \cdot A)^{-1}$ is matrix $(A^T \cdot A)$ inverse, a_n and b_n can be obtained from Eq. (13).

Acknowledgments

This work was jointly supported by the National Key Basic Research Program of China (Grant No. 2015CB953702), the National Natural Science Foundation of China (NSFC) (Grant No. 91425303), the SAFEA Long-Term Projects of the 1000 Talent Plan for High-Level Foreign Experts (Grant No. WQ20141100224), and the National Nature Science Foundation of China (Grant No. 41601358). The field data were collected from Watershed Allied Telemetry Experimental Research (WATER) provided by Cold and Arid Regions Sciences

Data Center at Lanzhou, and we gratefully acknowledge the efforts of researchers who contributed to the field measurements. The author would like to thank the reviewers for their valuable comments and suggestions.

References

1. S. B. Idso, J. K. Aase, and R. D. Jackson, "Net radiation—soil heat flux relations as influenced by soil water content variations," *Boundary-Layer Meteorol.* **9**(1), 113–122 (1975).
2. B. E. Clothier et al., "Estimation of soil heat flux from net radiation during the growth of alfalfa," *Agric. For. Meteorol.* **37**(4), 319–329 (1986).
3. W. P. Kustas and C. S. T. Daughtry, "Estimation of the soil heat flux/net radiation ratio from spectral data," *Agric. For. Meteorol.* **49**(3), 205–223 (1990).
4. K. Wilson et al., "Energy balance closure at FLUXNET sites," *Agric. For. Meteorol.* **113**(1–4), 223–243 (2002).
5. B. G. Heusinkveld et al., "Surface energy balance closure in an arid region: role of soil heat flux," *Agric. For. Meteorol.* **122**(1–2), 21–37 (2004).
6. G. Wang et al., "Observation analysis of land-atmosphere interactions over the Loess Plateau of northwest China," *J. Geophys. Res. Atmos.* **115**(D7), D00K17 (2010).
7. C. Liebethal, B. Huwe, and T. Foken, "Sensitivity analysis for two ground heat flux calculation approaches," *Agric. For. Meteorol.* **132**(3–4), 253–262 (2005).
8. T. Murray and A. Verhoef, "Moving towards a more mechanistic approach in the determination of soil heat flux from remote measurements: I. A universal approach to calculate thermal inertia," *Agric. For. Meteorol.* **147**(1–2), 80–87 (2007).
9. A. Verhoef et al., "Spatio-temporal surface soil heat flux estimates from satellite data; results for the AMMA experiment at the Fakara (Niger) supersite," *Agric. For. Meteorol.* **154–155**, 55–66 (2012).
10. B. J. Choudhury, S. B. Idso, and R. J. Reginato, "Analysis of an empirical model for soil heat flux under a growing wheat crop for estimating evaporation by an infrared-temperature based energy balance equation," *Agric. For. Meteorol.* **39**(4), 283–297 (1987).
11. W. P. Kustas, C. S. T. Daughtry, and P. J. Van Oevelen, "Analytical treatment of the relationships between soil heat flux/net radiation ratio and vegetation indices," *Remote Sens. Environ.* **46**(3), 319–330 (1993).
12. J. A. Santanello and M. A. Friedl, "Diurnal covariation in soil heat flux and net radiation," *J. Appl. Meteorol.* **42**(6), 851–862 (2003).
13. Z. Su, "The surface energy balance system (SEBS) for estimation of turbulent heat fluxes," *Hydrol. Earth Syst. Sci.* **6**(1), 85–100 (2002).
14. W. Bastiaanssen et al., "A remote sensing surface energy balance algorithm for land (SEBAL). 1. Formulation," *J. Hydrol.* **212**, 198–212 (1998).
15. R. J. Reginato, R. D. Jackson, and P. J. Pinter Jr., "Evapotranspiration calculated from remote multispectral and ground station meteorological data," *Remote Sens. Environ.* **18**(1), 75–89 (1985).
16. T. Murray and A. Verhoef, "Moving towards a more mechanistic approach in the determination of soil heat flux from remote measurements: II. Diurnal shape of soil heat flux," *Agric. For. Meteorol.* **147**(1–2), 88–97 (2007).
17. C. Cammalleri, G. La Loggia, and A. Maltese, "Critical analysis of empirical ground heat flux equations on a cereal field using micrometeorological data," *SPIE Eur. Remote Sens.* **7472**, 747225 (2009).
18. H. S. Carslaw and J. C. Jaeger, "Conduction of heat in solids," pp. 64–70, Oxford at the Clarendon Press (1959)
19. W. Van Wijk and V. De Vries, "Periodic temperature variations in a homogeneous soil," in *Physics of Plant Environment*, W. R. van Wijk, Ed., pp. 102–143, John Wiley & Sons, New York (1963).
20. R. Horton and P. J. Wierenga, "Estimating the soil heat flux from observations of soil temperature near the surface," *Soil Sci. Soc. Am. J.* **47**(1), 14–20 (1983).

21. X. Li et al., "Heihe watershed allied telemetry experimental research (HiWATER): scientific objectives and experimental design," *Bullet. Am. Meteorol. Soc.* **94**(8), 1145–1160 (2013).
22. G. D. Cheng, *Heihe River Basin: Integrated Study of the Water-Ecosystem-Economy*, p. 581, Science Press Ltd., China (2009)
23. S. Liu et al., "Measurements of energy and water vapor fluxes over different surfaces in the Heihe River Basin, China," *Hydrol. Earth Syst. Sci. Discuss.* **7**(6), 8741–8780 (2010).
24. S. M. Liu et al., "A comparison of eddy-covariance and large aperture scintillometer measurements with respect to the energy balance closure problem," *Hydrol. Earth Syst. Sci.* **15**(4), 1291–1306 (2011).
25. B. Tang et al., "Generalized split-window algorithm for estimate of land surface temperature from Chinese geostationary FengYun meteorological satellite (FY-2C) data," *Sensors* **8**(2), 933–951 (2008)
26. B. Tang and Z. L. Li, "Algorithms for surface albedo, emissivity and temperature from geostationary satellite," CEOP-AEGIS Deliverable Report De2.3, Ed., p. 2125, University of Strasbourg, France, ISSN 2118-7843 (2011).
27. H. R. Ghafarian et al., "Reconstruction of cloud-free time series satellite observations of land surface temperature," *EARSel eProc.* **11**, 123–131 (2012)
28. H. R. Ghafarian, "Reconstruction of gap-free time series satellite observations of land surface temperature to model spectral soil thermal admittance," PhD Thesis, University of Twente, Netherlands (2015)
29. M. Massimo, J. Li, and J. Colin, "Coordinated Asia-European long-term observing system of Qinghai-Tibet Plateau hydro-meteorological processes and the Asian-monsoon system with ground satellite image data and numerical Simulations (CEOP-AEGIS)," Final Report, Ed., 60p, University of Strasbourg, France ISSN 2118-7843 (2014).
30. Q. Liu et al., "Analysis of spatial distribution and multi-year trend of the remotely sensed soil moisture on the Tibetan Plateau," *Sci. China Earth Sci.* **56**(12), 2173–2185 (2013).
31. J. Shi et al., "A parameterized multifrequency-polarization surface emission model," *IEEE Trans. Geosci. Remote Sens.* **43**(12), 2831–2841 (2005).
32. J. C. Shi et al., "Physically based estimation of bare-surface soil moisture with the passive radiometers," *IEEE Trans. Geosci. Remote Sens.* **44**(11), 3145–3153 (2006).
33. M. Menenti et al., "Mapping agroecological zones and time lag in vegetation growth by means of Fourier analysis of time series of NDVI images," *Adv. Space Res.* **13**(5), 233–237 (1993).
34. W. Verhoef, M. Menenti, and S. Azzali, "Cover A colour composite of NOAA-AVHRR-NDVI based on time series analysis (1981–1992)," *Int. J. Remote Sens.* **17**(2), 231–235 (1996).
35. L. Jia and J. Zhou, *The Cloud-Free NDVI Data from 2001 to 2011 in the Heihe River Basin*, Heihe Plan Science Data Center (2013).
36. W. G. M. Bastiaanssen et al., "Surface energy balance and actual evapotranspiration of the transboundary Indus Basin estimated from satellite measurements and the ETLook model," *Water Resour. Res.* **48**(11), W11512 (2012).
37. W. Shangguan et al., "A China data set of soil properties for land surface modeling," *J. Adv. Model. Earth Syst.* **5**(2), 212–224 (2013).
38. J. Wang et al., "An overview of the HEIFE experiment in the People's Republic of China," in *Exchange Processes at the Land Surface for a Range of Space and Time Scales*, Vol. **212**, pp. 397–403, IAHS Publications (1993)
39. Y. Hu et al., "Some achievements in scientific research during HEIFE," *Plateau Meteorol.* **13**(3), 225–236 (1994)
40. X. Li et al., "Simultaneous remote sensing and ground-based experiment in the Heihe River Basin: scientific objectives and experiment design," *Adv. Earth Sci.* **23**(9), 897–914 (2008)
41. X. Li et al., "Watershed allied telemetry experimental research," *J. Geophys. Res. Atmos.* **114**, D22103 (2009).
42. X. Li et al., "Observing and modeling the catchment scale water cycle preface," *Hydrol. Earth Syst. Sci.* **15**(2), 597–601 (2011).
43. G. Cheng et al., "Integrated study of the water-ecosystem–economy in the Heihe River Basin," *Nat. Sci. Rev.* **1**(3), 413–428 (2014).

44. N. N. Li, L. Jia, and J. Lu, "An improved algorithm to estimate the surface soil heat flux over a heterogeneous surface: a case study in the Heihe River Basin," *Sci. China Earth Sci.* **58**(7), 1169–1181 (2015).
45. O. Johansen, "Thermal conductivity of soils," DTIC Document (1977).
46. L. Gong et al., "Sensitivity of the Penman-Monteith reference evapotranspiration to key climatic variables in the Changjiang (Yangtze River) basin," *J. Hydrol.* **329**(3–4), 620–629 (2006).
47. A. Mousivand et al., "Global sensitivity analysis of the spectral radiance of a soil-vegetation system," *Remote Sens. Environ.* **145**(0), 131–144 (2014).
48. M. S. McKenney and N. J. Rosenberg, "Sensitivity of some potential evapotranspiration estimation methods to climate change," *Agric. For. Meteorol.* **64**(1–2), 81–110 (1993).
49. R. Goyal, "Sensitivity of evapotranspiration to global warming: a case study of arid zone of Rajasthan (India)," *Agric. Water. Manage* **69**(1), 1–11 (2004).
50. R. H. McCuen, *A Sensitivity and Error Analysis of Procedures Used for Estimating Evaporation*, Wiley Online Library (1974).
51. K. E. Saxton, "Sensitivity analyses of the combination evapotranspiration equation," *Agric. Meteorol.* **15**(3), 343–353 (1975).
52. K. Beven, "A sensitivity analysis of the Penman-Monteith actual evapotranspiration estimates," *J. Hydrol.* **44**(3–4), 169–190 (1979).
53. F. Hupet and M. Vanclooster, "Effect of the sampling frequency of meteorological variables on the estimation of the reference evapotranspiration," *J. Hydrol.* **243**(3–4), 192–204 (2001).
54. G. Rana and N. Katerji, "A measurement based sensitivity analysis of the Penman-Monteith actual evapotranspiration model for crops of different height and in contrasting water status," *Theor. Appl. Climatol.* **60**(1–4), 141–149 (1998).
55. G. Y. Qiu, T. Yano, and K. Momii, "An improved methodology to measure evaporation from bare soil based on comparison of surface temperature with a dry soil surface," *J. Hydrol.* **210**(1–4), 93–105 (1998).
56. T. Sauer et al., "Errors in heat flux measurement by flux plates of contrasting design and thermal conductivity," *Vadose Zone J.* **2**(4), 580–588 (2003).
57. T. J. Sauer, T. E. Ochsner, and R. Horton, "Soil heat flux plates: heat flow distortion and thermal contact resistance," *Agron. J.* **99**(1), 304–310 (2007)
58. T. E. Ochsner, T. J. Sauer, and R. Horton, "Field tests of the soil heat flux plate method and some alternatives," *Agron. J.* **98**(4), (2006).
59. S. Lu et al., "A general approach to estimate soil water content from thermal inertia," *Agric. For. Meteorol.* **149**(10), 1693–1698 (2009).

Nana Li received her PhD in remote sensing science and technology from the University of Chinese Academy of Sciences in 2015. She is a postdoctoral researcher in hydrological remote sensing at Tsinghua University. Her current research interests include remote sensing for hydrology, terrestrial water cycle, and land surface energy balance. She is a member of SPIE.

Li Jia received her PhD in environmental science from Wageningen University of The Netherlands in 2004. She is a professor at the State Key Laboratory of Remote Sensing Science, jointly sponsored by the Institute of Remote Sensing and Digital Earth of Chinese Academy of Sciences and Beijing Normal University. Her research interests are on the study of earth observation and its applications in hydrometeorology, water resources, agriculture, and climate change.

Jing Lu received her PhD from the University of Chinese Academy of Sciences in 2014. She is a research assistant at the Institute of Remote Sensing and Digital Earth of Chinese Academy of Sciences. Her research interests include evapotranspiration estimation with remote sensing, land surface energy balance, and so on.

Massimo Menenti received his PhD from the Wageningen Agriculture University of The Netherlands in 1984. He is a full professor in Delft University of Technology of The

Netherlands. He is also a professor at the Institute of Remote Sensing and Digital Earth of Chinese Academy. His research interests focus on the use of earth observation to study the hydrology and hydrometeorology of the global land surface.

Jie Zhou received his PhD from the University of Chinese Academy of Sciences in 2016. He is a research assistant at the Institute of Remote Sensing and Digital Earth of Chinese Academy of Sciences. His research interests include time series analysis and reconstruction of remote sensing data, vegetation dynamic and drought monitoring study with remote sensing, and so on.